Journal of Solid State Chemistry 213 (2014) 210–217

Contents lists available at ScienceDirect

Journal of Solid State Chemistry

journal homepage: www.elsevier.com/locate/jssc

Effect of polyvinylpyrrolidone on mesoporous silica morphology and esterification of lauric acid with 1-butanol catalyzed by immobilized enzyme

Jinyu Zhang, Guowei Zhou *, Bin Jiang, Minnan Zhao, Yan Zhang

Key Laboratory of Fine Chemicals in Universities of Shandong, School of Chemistry and Pharmaceutical Engineering, Qilu University of Technology, Jinan 250353, Shandong, People's Republic of China

ARTICLE INFO

Article history:
Received 19 November 2013
Received in revised form
26 February 2014
Accepted 2 March 2014
Available online 12 March 2014

Keywords:
Morphology evolution
Polyvinylpyrrolidone
Curved mesoporous silica
Immobilized lipase
Esterification

ABSTRACT

Mesoporous silica materials with a range of morphology evolution, i.e., from curved rod-shaped mesoporous silica to straight rod-shaped mesoporous silica, were successfully prepared using polyvinylpyrrolidone (PVP) and triblock copolymer as dual template. The effects of PVP molecular weight and concentration on mesoporous silica structure parameters were studied. Results showed that surface area and pore volume continuously decreased with increased PVP molecular weight. Mesoporous silica prepared with PVP K30 also possessed larger pore diameter, interplanar spacing (d_{100}), and cell parameter (a_0) than that prepared with PVP K15 and PVP K90. In addition, with increased PVP concentration, d_{100} and a_0 continuously decreased. The mechanism of morphology evolution caused by the change in PVP concentration was investigated. The conversion rate of lauric acid with 1-butanol catalyzed by immobilized *Porcine pancreatic* lipase (PPL) was also evaluated. Results showed that PPL immobilized on amino-functionalized straight rod-shaped mesoporous silica maintained 50% of its esterification conversion rate even after five cycles of use with a maximum conversion rate was about 90.15%.

1. Introduction

Organic acid esters are widely used as chemical intermediates for the synthesis of biodiesel [1,2], textile, cosmetic, flavor, and fragrant compounds because of their great practical applications in various industries. Generally, esterification reactions of carboxylic acids with alcohols are commercially catalyzed using heterogeneous [1–4] and homogeneous catalysts [5,6]. Immobilized enzymes, as heterogeneous catalysts, currently attract considerable attention because of their considerable physiological and industrial significance [3,4,7]. These enzymes have many advantages, such as high selectivity and specificity for substrate, high stability, reusability, and applicability to extreme conditions [8]. However, the stability and reusability of immobilized enzymes are closely linked with a suitable support.

Ordered mesoporous silica has been proposed as a suitable support for enzyme immobilization [9] and is synthesized with a surfactant as template using supramolecular-template methods. Polyvinylpyrrolidone (PVP) is a common non-ionic surfactant that can be used to form metal–inorganic composite particles [10–12], hierarchical compounds [13–15], membranes [16], fibers [17–21], and core–shell mesoporous nanoparticles [22–24]. Many studies have reported mesoporous silica materials with the morphology of hollow spheres [23,24], spheres [25], and fibers by PVP-assisted reaction. However, only a few works have described mesoporous silica rod prepared using PVP as template. Zhu et al. [24] successfully synthesized hollow mesoporous silica spheres with uniform size and morphology, where PVP contributes to the formation of a hollow structure. Rod-shaped mesoporous silica with open-framework structure have received much attention in the past decade as potential materials for drug delivery systems, catalyst supports, and sensors because of their ordered mesochannels, high BET surface area, large pore volume, uniform porosity, stable aqueous dispersion, and excellent biocompatibility [26,27]. Huang et al. [28] proved that rod-shaped mesoporous silica nanoparticles are superior to their spherical counterparts in drug delivery applications. Rod-shaped mesoporous silica are advantageous over spherical ones. For example, rod-shaped mesoporous silica with short pore channels possess remarkably improved immobilization abilities for enzymes because of the doubled open mouth at the rod terminal, short diffusion paths, fast adsorption, and ease in mass transfer. Butyl laurate is mainly used to prepare flavors and fragrances because of its fruit- or peanut-like aroma. Brahmkhatri et al. [29] synthesized butyl laurate catalyzed by $H_3PW_{12}O_{40}$

* Corresponding author. Tel.: +86 531 89631696.
E-mail addresses: guoweizhou@hotmail.com, gwzhou@qlu.edu.cn (G. Zhou).

http://dx.doi.org/10.1016/j.jssc.2014.03.004
0022-4596/

supported on MCM-41. Barros et al. [30] also studied the esterification of lauric acid with butanol over mesoporous materials. Results showed that ZnO/SBA-15 and MgO/SBA-15 led to high esterification yields at ambient pressure.

In this study, mesoporous silica materials including curved rod-shaped mesoporous silica (CRMS) and straight rod-shaped mesoporous silica (SRMS) were successfully synthesized using PVP and P123 as co-template by varying different reaction parameters such as the mole ratio of PVP to P123 and the molecular weight of PVP. We investigated the characteristics of mesoporous silica size, morphology, and structure, which significantly influenced its physical and chemical properties, as well as its applications in enzyme immobilization. Esterification of lauric acid with 1-butanol catalyzed by immobilized *Porcine pancreatic* lipase (PPL) (SRMS-S2-PPL and NH-SRMS-S2-PPL) was then investigated.

2. Experimental

2.1. Materials

Poly(ethylene glycol)-block-poly(propyleneglycol)-block-poly (ethylene glycol) (P123), PPL, (3-aminopropyl)triethoxysilane (APTES) (98%), bovine serum albumin (BSA), Coomassie brilliant blue G-250, and triacetin ($C_9H_{14}O_6$, 99%) were purchased from Sigma-Aldrich Co. Polyvinylpyrrolidone (PVP (K15, K30, and K90)), tetraethoxysilane (TEOS), and lauric acid were used as received from Sinopharm Chemical Reagent Co., Ltd. Other chemicals were of analytical grade and were all obtained from Tianjin Chemical Agent Co. (China).

2.2. Synthesis of mesoporous silica materials and amino-functionalization

CRMS and SRMS were prepared by tuning the molar ratio of the two structure-directing agents to obtain ordered hexagonal-like mesoporous channels and rod-shaped silica. To obtain an appropriate concentration ratio, the concentration of PVP (K30) was varied while fixing the amount of P123. The molar ratio of TEOS:P123:PVP:HCl:H_2O was 1:0.01671:(0, 0.0116, 0.058, 0.116, 0.174):5.814:190.0, and the samples were designated as CRMS-S0, CRMS-S1, SRMS-S2, SRMS-S3, and CRMS-S4. Samples synthesized at a molar ratio of 1:0.116 (P123:PVP) were designated as SRMS-S5 (PVP K15) and CRMS-S6 (PVP K90). About 1.0 g of P123 was placed at the bottom of a beaker and mixed with 30.0 g of aqueous HCl solution (2.0 mol L^{-1}) and 7.5 g of deionized water. After initial stirring for 2 h, the solution became clear. Then, 2.15 g of TEOS was added at a stirring rate of 500 rpm throughout the reaction period. Certain amounts of PVP were then sequentially added to the solution, which was stirred at 308 K for 24 h. The solution along with the produced precipitate was transferred to an autoclave and heated at 373 K for another 24 h. The product was filtered, washed three times with deionized water, and calcined at 823 K in flowing air for 6 h to remove surfactant. The functional group used to functionalize CRMS and SRMS came from APTES, and the functionalization procedure was performed by postsynthesis-grafting method [31–33]. The obtained samples were designated as NH-CRMS or NH-SRMS (NH-CRMS-S0, NH-CRMS-S1, NH-SRMS-S2, NH-SRMS-S3, NH-CRMS-S4, NH-SRMS-S5, and NH-CRMS-S6).

2.3. Immobilization of PPL and activity assays

PPL immobilization onto SRMS-S2 or NH-SRMS-S2 and activity assay were carried out according to our previous work [8]. Final samples after PPL immobilization were designated as SRMS-S2-PPL and NH-SRMS-S2-PPL. The amount (P, mg g^{-1}) of PPL immobilization and activity (E_a, U g^{-1}) of immobilized PPL was obtained.

2.4. Esterification procedure

Ester synthesis in *n*-hexane (10 mL) and 3 mL of phosphate buffer solution (pH 7.0) was carried out in a 100 mL three-necked flask using lauric acid (0.2 mol L^{-1}, 0.4 g) and 1-butanol (0.4 mol L^{-1}, 0.296 g) as substrates. SRMS-S2-PPL or NH-SRMS-S2-PPL (0.06 g) was also added to the mixture. Esterification was then carried out at 313 K with constant stirring using a magnetic stirrer.

Results of the reaction were determined by measuring the lauric acid conversion rate (α, %) according to reference reports [34].

2.5. Characterization

Small-angle X-ray powder diffraction (SAXRD) patterns were recorded in the 2θ range 0.5°–3° at a step size of 0.02° with a Bruker D8 advance diffractometer, using Cu$K\alpha$ radiation (30 kV, 30 mA, λ=0.1541 nm). Field emission scanning electron microscopy (FESEM) micrographs were observed by a SUPRA^{TM} 55 microscope operating at an accelerating voltage of 5 kV. Transmission electron microscopy (TEM) micrographs were obtained on a JEM-1400 microscope with an acceleration voltage of 120 kV. The dry-weight-based C, H, and N contents were determined using a Vario ELIII elemental analyzer with the oxygen content calculated by the mass difference. N_2 adsorption–desorption apparatus (Micromeritics, TriStar 3020) was used to determine surface areas, pore volumes, and pore size distributions. The surface areas were calculated by the Brunauer–Emmett–Teller (BET) method. The pore diameters were estimated from the desorption branches of the isotherms based on the Barrett–Joyner–Halenda (BJH) model. Small-angle X-ray scattering (SAXS) experiments were performed using a SAXSess mc^2 system (Anton Paar) with a Cu$K\alpha$ radiation (0.1542 nm) operating at 40 kV and 50 mA. The sample-to-detector distance was 0.26 m, and the test temperature was 308 K. Scattering curves of P123/PVP/SiO_2 sols with different PVP concentrations were recorded for q ranging from 0.2 nm^{-1} to 1.5 nm^{-1}.

3. Results and discussion

3.1. The structural characteristics

3.1.1. SAXRD analysis

Fig. 1a shows the SAXRD patterns of samples synthesized with different P123:PVP molar ratios. All samples had three well-resolved Bragg diffraction peaks unambiguously indexed as the (1 0 0), (1 1 0), and (2 0 0) reflection of a hexagonal symmetry structure ($p6mm$) [35,36]. The interplanar spacings (d_{100}) values and cell parameter ($a_0=2d/3^{1/2}$) are summarized in Table 1. With increased PVP concentration, diffraction peak position moved to a higher angle side and relative intensities increased. However, the relatively wide and similar peak of the sample synthesized with P123 as a template was located at the highest angle, indicating relatively poor structural ordering. In addition, the structural ordering of samples templated by mixed P123/PVP surfactants increased, and a_0 and d_{100} continuously decreased with increased PVP. The SAXRD patterns of amino-functionalized samples are shown in Fig. 1b. All samples had three peaks and structural ordering, and a_0 and d_{100} decreased with increased PVP, indicating that the hexagonal symmetry structure did not change after functionalization. The structural ordering of amino-functionalized samples was reduced to a certain extent. Compared with CRMS-S0,

NH-CRMS-S0 had larger d_{100} and a_0, and other samples exhibited the opposite. In addition, compared with PVP (K15, 10000) and PVP (K90, 360000), SRMS-S3 synthesized with PVP (K30, 40000) had narrower peaks (Fig. S1, Supporting information), indicating better structural ordering. SRMS-S2 also had narrower peaks than CRMS-S1, SRMS-S3, and CRMS-S4. The peaks of NH-SRMS-S2 were also narrower than other functionalized samples. Thus, a molar ratio of 1:0.058 and PVP (K30) were the best conditions.

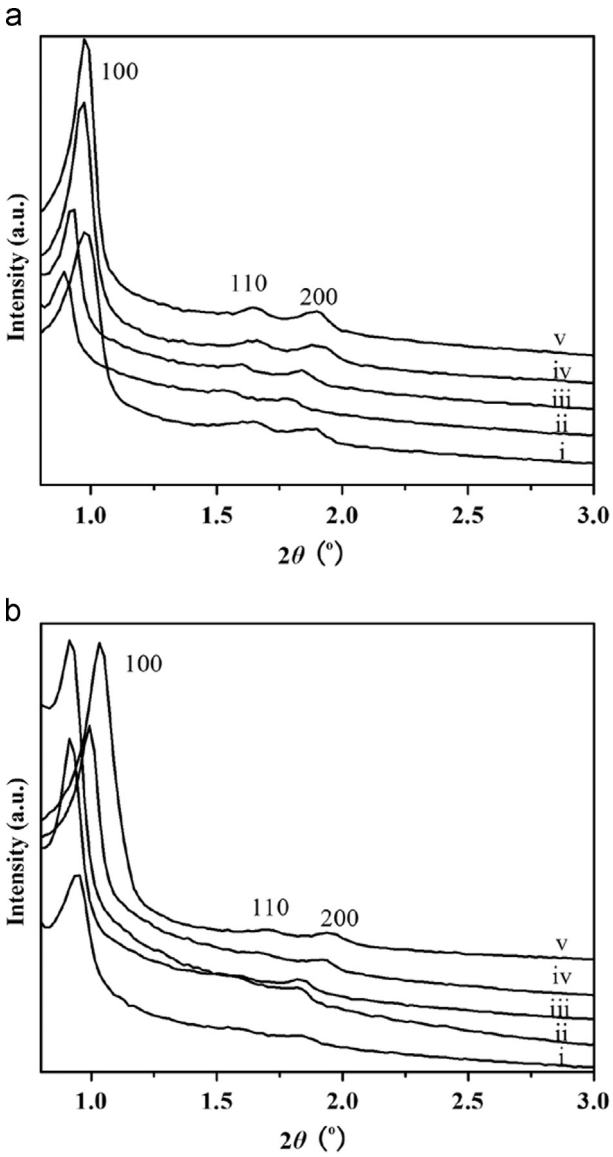

Fig. 1. SAXRD patterns of (a) CRMS or SRMS and (b) NH-CRMS or NH-SRMS: (i) CRMS-S0, (ii) CRMS-S1, (iii) SRMS-S2, (iv) SRMS-S3, and (v) CRMS-S4.

3.1.2. TEM images

CRMS and SRMS exhibited arrays of long-range mesoporous channels with an average pore diameter of around 5 nm to 7 nm (Fig. 2), consistent with nitrogen adsorption–desorption measurements. The morphology of CRMS-S1, CRMS-S4, and CRMS-S6 (Fig. S2d, Supporting information) had a certain curvature, whereas SRMS-S2, SRMS-S3, and SRMS-S5 (Fig. S2c, Supporting information) presented straight characteristics. The morphology of CRMS-S0 showed slightly curved rod-shaped silica with an irregular shape, as shown in Fig. S2a and b (Supporting information).

3.1.3. SEM images

To determine the relationship of morphology evolution with PVP concentration, CRMS and SRMS were further studied by FESEM. Results showed that CRMS-S1 (Fig. 3a) and CRMS-S4 (Fig. 3d) were slightly curved rod-shaped mesoporous silica, whereas SRMS-S2 (Fig. 3b) and SRMS-S3 (Fig. 3c) were straight rod-shaped mesoporous silica. When the P123/PVP molar ratio was 1:0.0116 or 1:0.174, CRMS-S1 and CRMS-S4 had an average length of 1 μm, but the widths were 200 and 300 nm, respectively. As shown in Fig. 3a and d, slightly curved rod-shaped mesoporous silica appeared to aggregate to some extent. When the P123/PVP molar ratio was 1:0.058 or 1:0.116, the length decreased to 800 nm with increased width to around 500 nm. Compared with SRMS-S3, SRMS-S2 was uniform without aggregation. Moreover, PVP concentration influenced the morphology of CRMS or SRMS; hence, SRMS-S2 was the best sample.

3.1.4. Element analysis

A sample of SRMS-S2 is correctly shown in Table 2 as a material with a H content of 1.424% without C and N. This result indicated that the template agent P123 and PVP were completely removed during calcination. The element content of C, N, and H in NH-SRMS-S2 increased to 1.977%, 7.162%, and 2.297%, respectively, because of subsequent functionalization. A comparison of SRMS-S2-PPL and NH-SRMS-S2-PPL revealed that the contents of C, N, and H increased from 1.212%, 5.618%, and 2.287% to 2.805%, 9.808%, and 2.612%, respectively, which can be attributed to the appearance of PPL. These results confirmed that the aminopropyl group and PPL were located on RMS and NH-RMS.

Table 1
Prepared samples and their characterization results.

Sample	P123:PVP (molar ratio)	d_{100} (nm)	a_0 (nm)	2θ (°)	D[a] (nm)	S_{BET}[a] ($m^2\ g^{-1}$)	V[a] ($cm^3\ g^{-1}$)	T_p[b] (nm)
CRMS-S1	1:0.0116	9.90	11.43	0.892	5.97	637	0.80	5.46
SRMS-S2	1:0.058	9.53	11.00	0.926	5.40	615	0.73	5.60
SRMS-S3	1:0.116	9.10	10.51	0.970	5.32	615	0.73	5.19
CRMS-S4	1:0.174	9.07	10.48	0.973	5.34	620	0.73	5.14
NH-CRMS-S1	1:0.0116	9.69	11.19	0.911	5.94	252	0.42	5.25
NH-SRMS-S2	1:0.058	9.64	11.13	0.916	5.32	351	0.56	5.47
NH-SRMS-S3	1:0.116	9.00	10.39	0.981	5.28	277	0.44	5.11
NH-CRMS-S4	1:0.174	8.59	9.92	1.027	5.30	351	0.55	4.47
SRMS-S2-PPL	1:0.058				5.32	286	0.49	
NH-SRMS-S2-PPL	1:0.058				5.02	198	0.32	

[a] D, S_{BET}, and V stand for BET pore diameter, surface area, and pore volume, respectively.
[b] pore wall thickness as $T_p = a_0 - D$.

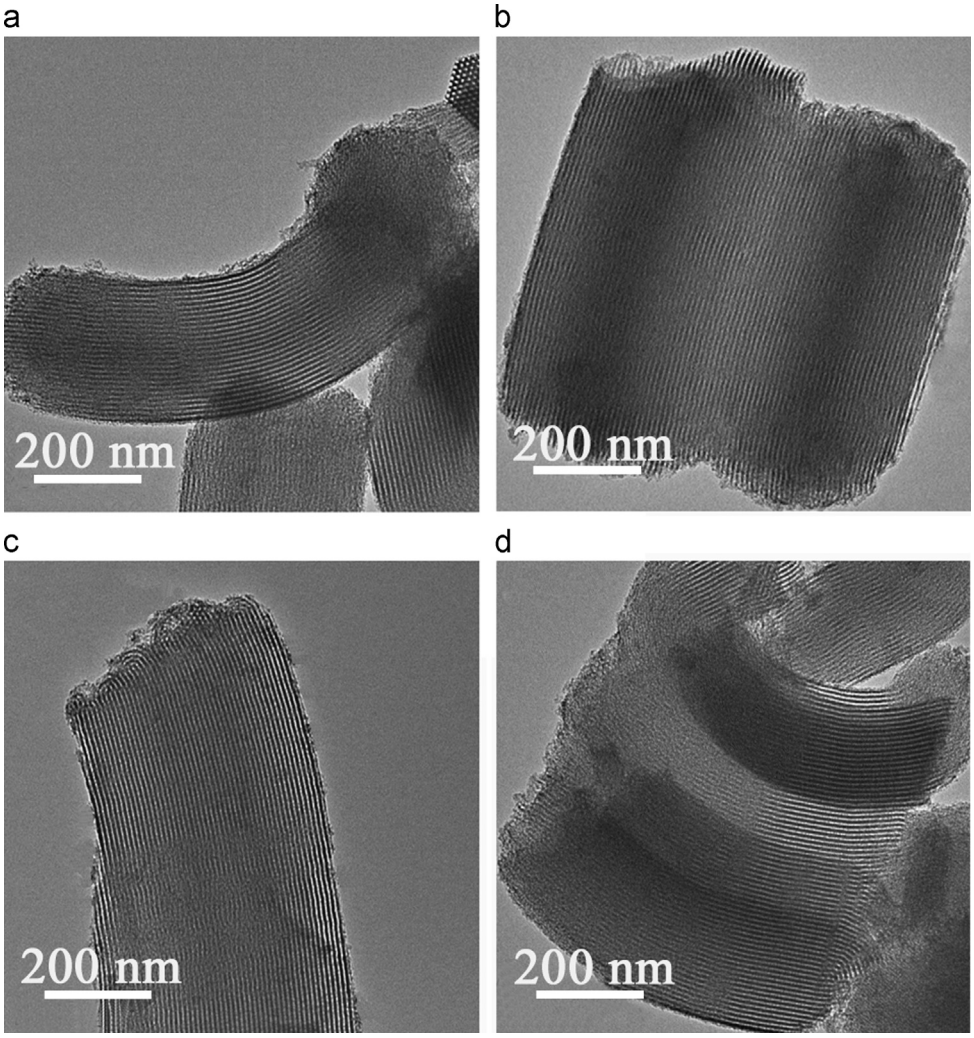

Fig. 2. TEM images of (a) CRMS-S1, (b) SRMS-S2, (c) SRMS-S3, and (d) CRMS-S4.

3.1.5. N_2 adsorption–desorption isotherms

The N_2 adsorption–desorption isotherms and the corresponding BJH pore size distribution curves of the samples are shown in Fig. 4. All samples exhibited type IV isotherms with H1-type hysteretic loops within a relative pressure (P/P_0) range of 0.50 to 0.80, which were related to a highly ordered mesoporous structure and cylindrical channels [37,38]. The mean value of pore diameter (D), surface area (S_{BET}), wall thickness (T_p), and pore volume (V) were evaluated in Table 1. D and S_{BET} initially decreased and then increased with increased PVP concentration, whereas T_p initially increased and then decreased. With increased PVP molecular weight, D and T_p had the same trend as the change in concentration, but S_{BET} and V decreased (Table S1, Supporting information). This result indicated that PVP played an important role in the formation of CRMS and SRMS, and that PVP molecular weight and concentration were important influencing factors. Textural parameters did not present a linear change with increased PVP concentration, which can be predicted by SEM. Notably, pore size distribution showed a narrow pore distribution (Fig. 4b). The pore size distribution of SRMS-S3 had a narrower range than those of SRMS-S5 and CRMS-S6 (Fig. S3, Supporting information), which meant higher structural ordering. The sample of SRMS-S2 displayed narrower pore size distribution than CRMS-S1, SRMS-S3, and CRMS-S4, consistent with SAXRD results. Compared with CRMS and SRMS, the S_{BET}, T_p, and V of NH-CRMS and NH-SRMS decreased, whereas the pore size irregularly varied. Consequently, most aminopropyl groups were located on the surface of CRMS and SRMS.

3.2. SAXS analysis of P123/PVP/SiO_2 sols with different PVP concentrations

Xu et al. [39] studied the effect of PVP on different microstructures of spherical PVP/SiO_2 sol particles by SAXS. They found that the PVP concentration has an important function in the SiO_2 sol process and the growth of SiO_2 clusters. To distinguish the formation of different P123–PVP structures, P123/PVP/SiO_2 sols formed using different P123–PVP mole ratios were tested to obtain the scattering curves (Fig. 5). The scattering vector amplitude q is defined as $q=4\pi\sin\theta/\lambda$, where θ is the scattering angle, and λ is the wavelength of the incident X-ray. The d spacing ($d=2\pi/q$) and a_0 ($a_0=2d/3^{1/2}$) can be obtained from q. The SAXS profiles reveal that all samples have a strong scattering peak centered at $q\approx 0.56\ nm^{-1}$ and correspond to the (10) reflection from the hexagonal sols with different peak intensities and widths [40]. Based on calculations, $d=11.22$ nm and $a_0=12.96$ nm, which were all greater than d and a_0 from XRD analysis because of structural shrinkage following the removal of P123/PVP template agents. The results suggest that P123, TEOS, and PVP interact with each other in TEOS hydrolysis to form hexagonal P123/PVP/SiO_2 sols, and PVP

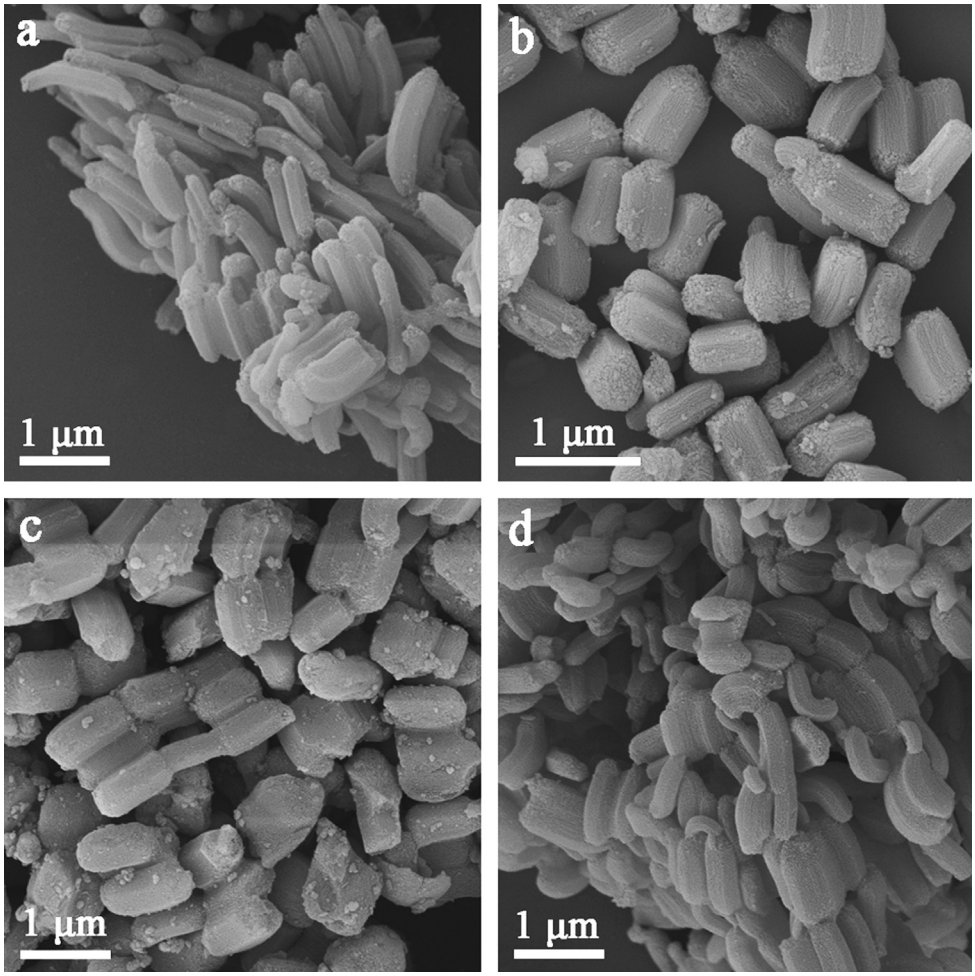

Fig. 3. FESEM images of (a) CRMS-S1, (b) SRMS-S2, (c) SRMS-S3, and (d) CRMS-S4.

Table 2
Elemental contents of (a) SRMS-S2, (b) NH-SRMS-S2, (c) SRMS-S2-PPL, and (d) NH-SRMS-S2-PPL.

Sample	Element		
	N (wt%)	C (wt%)	H (wt%)
SRMS-S2	0	0	1.424
NH-SRMS-S2	1.977	7.162	2.297
SRMS-S2-PPL	1.212	5.618	2.287
NH-SRMS-S2-PPL	2.805	9.808	2.612

concentration is important in the structural ordering and parameters [39].

3.3. Mechanism for the formation of CRMS and SRMS

The possible mechanism of such structural evolution may be related to the varied PVP concentration (Fig. 6). PVP is an amphiphilic molecule with a polyvinyl backbone and pyrrolidone group as hydrophobic and hydrophilic groups, respectively. This molecule is a long chain polymer with a random coil structure that has strong selective adsorption [41,42] and reduces the hydrolysis and condensation rates of TEOS [39]. The SAXS results revealed that P123, TEOS, and PVP interact with each other in TEOS hydrolysis to form hexagonal P123/PVP/SiO_2 sols. To describe the morphological evolution of the samples, TEOS was omitted in the initial part of the mechanism. The "necklace model" [14] states that the dissolution of a small number of PVP molecules in the P123/TEOS hydrolysis solution encloses a series of P123 spherical micelles with PVP molecular chains through the hydrogen bonding of silanol groups on the particle surface with the electronegative inner amide of PVP side chain [39]. The amount of PVP was relatively low, and the PVP molecules were separately surrounded by the mesophase, which were not sufficient to form a continuous layer and restrain the growth of the mesophase radially. Curved and rod-shaped P123/PVP/SiO_2 complex sols with 2D hexagonal mesophase surrounded by PVP molecule chains were formed [43,44]. Slightly curved and rod-shaped silica with smaller D and larger T_p were obtained because of the small restrictive power of PVP molecular chains. Therefore, curved CRMS-S1 with a high aspect ratio was formed because of the main structure-directing agent of P123, such as CRMS-S0 prepared only by P123. At higher PVP concentrations, more PVP molecule chains were adsorbed on P123 rod-shaped micelles and hexagonal aggregation, forming a continuous layer, similar to a colloid, to inhibit the growth of P123/PVP/SiO_2 sol in all directions [45,46]. Thus, the dimension of mesoporous silica increased radially and decreased horizontally because of the large restrictive power of PVP molecular chains, which resulted in straight rod-shaped silica CRMS-S2 and CRMS-S3 with low aspect ratios [47]. Further increase in the PVP concentration dissolved more PVP into the P123/TEOS hydrolysis solution for the adsorption on P123 rod-shaped micelles [48]. The excess PVP self-assembled with P123 into compound spherical micelles or with P123/TEOS hydrolysis solution into curved rod-shaped micelles and hexagonal compound aggregation of P123/PVP/SiO_2 sol because of the affinity between the hydrophilic groups [48]. This phenomenon yielded curved CRMS-S4 with high

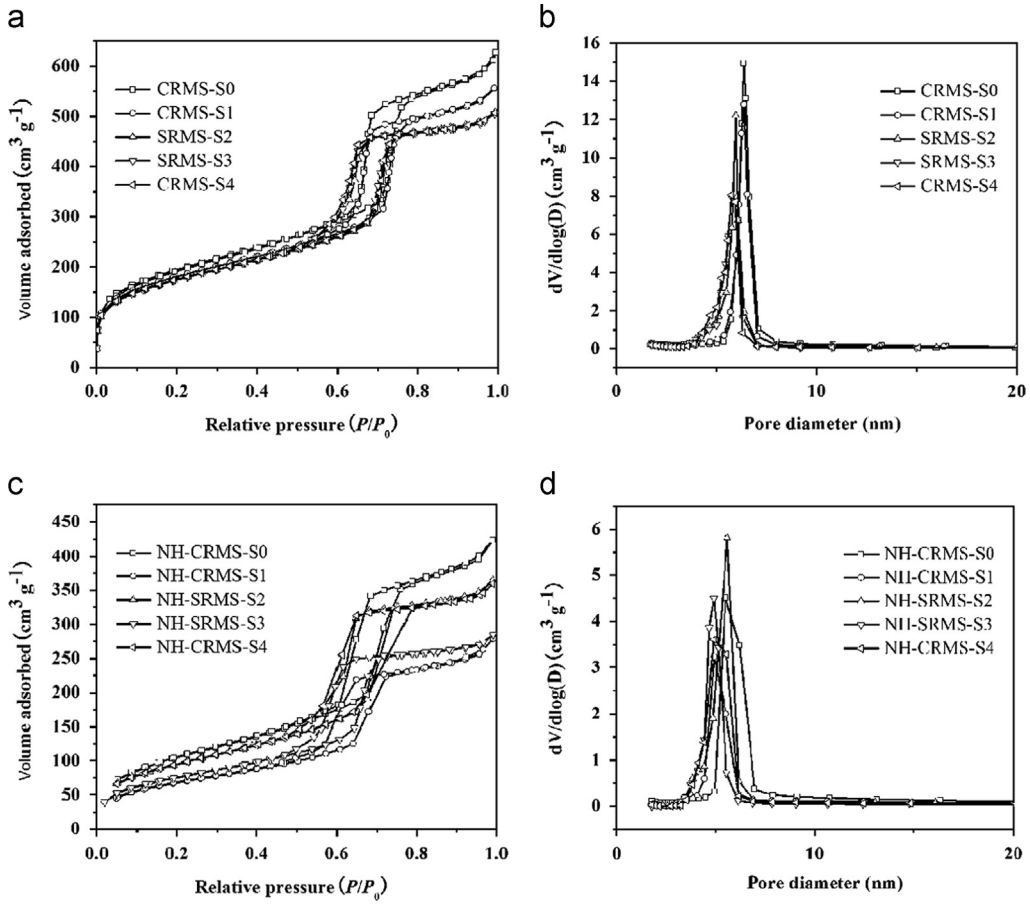

Fig. 4. N_2 adsorption–desorption isotherms (a) and (c) and corresponding BJH pore size distribution curves (b, d) of CRMS, SRMS, NH-CRMS, and NH-SRMS.

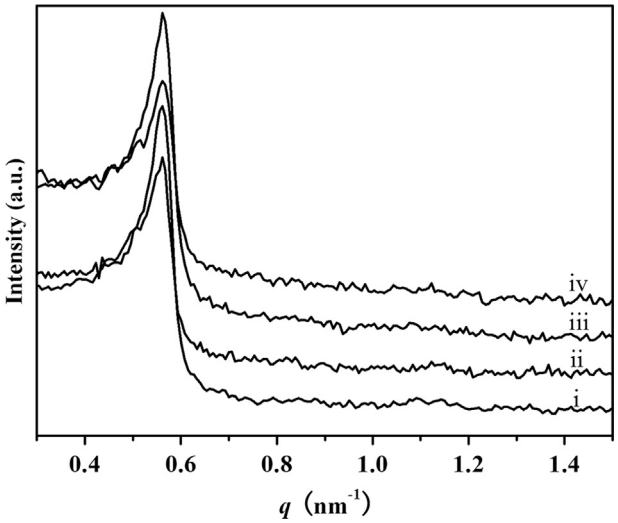

Fig. 5. SAXS curves of P123/PVP/SiO_2 sols formed with different P123:PVP mole ratios: (i) 1:0.0116, (ii) 1:0.058, (iii) 1:0.116, and (iv) 1:0.174.

aspect ratio. P123 was the main structure-directing agent, and the curvature phenomenon recurred. Compared with CRMS-S1, the length of CRMS-S4 was uneven, and the amount of irregular rod-shaped particles increased. After TEOS whole hydrolysis and condensation, as well as calcination of the as-synthesized products, PVP and P123 were removed without destroying the mesoporous SiO_2 2D hexagonal arrangement.

3.4. Loading amounts and activities of immobilized PPL

Table 1 shows that NH-SRMS-S2-PPL had smaller S_{BET}, D, and V than SRMS-S2-PPL. In addition, SRMS-S2-PPL had smaller S_{BET}, D, and V than SRMS-S2. Most PPLs were located in the pore channel of RMS, CRMS, and SRMS. PPL also had minimal effect on the structure of well-ordered hexagonal arrangements (Fig. S4, Supporting information). The effect of temperature and medium pH on the activity of SRMS-S2-PPL and NH-SRMS-S2-PPL were investigated from 293 K to 333 K (Fig. S5, Supporting information) and 5.0 to 9.0 (Fig. S6, Supporting information), respectively. Notably, the optimum conditions of SRMS-S2-PPL were 308 K and pH 7.0, whereas those of NH-SRMS-S2-PPL were about 313 K and pH 8.0.

SRMS-S2 possessed good loading amounts of 45.2 mg g^{-1}, whereas that of NH-SRMS-S2 was 77.64 mg g^{-1}. The activity of NH-SRMS-S2-PPL (2337.71 U g^{-1}) was larger than that of SRMS-S2-PPL (1493.36 U g^{-1}) because of amino-functionalization. Enzyme molecules approached mesoporous materials through hydrogen bonding, which occurred between amino and carboxylic groups on the enzyme molecule, and surface silanols. With the incorporation of organosilanes, surface hydrophobicity increased, resulting in better enzyme immobilization within mesoporous structures because lipase had better affinity to hydrophobic supports.

3.5. Esterification of lauric acid with n-butanol by immobilized PPL catalysis

To overcome the equilibrium limitation, esterification of lauric acid with *n*-butanol catalyzed by SRMS-S2-PPL or NH-SRMS-S2-PPL

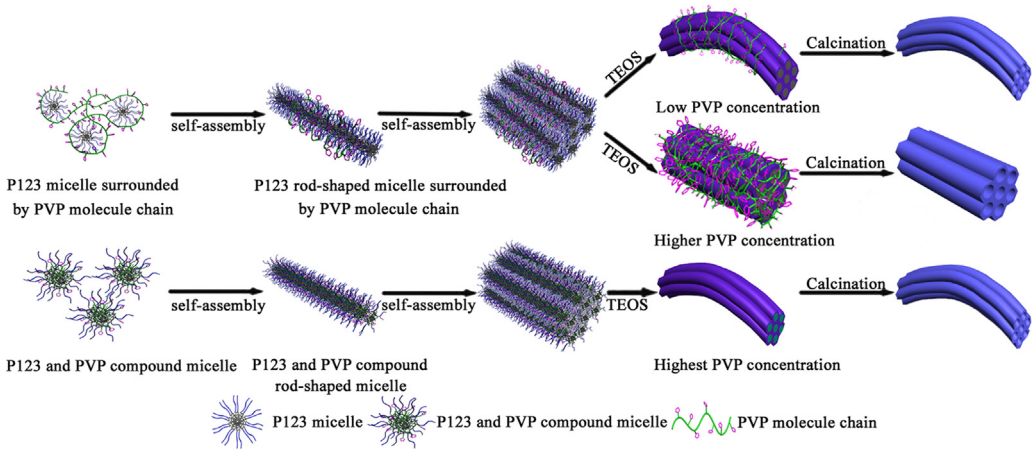

Fig. 6. The mechanism of morphology evolution between CRMS and SRMS.

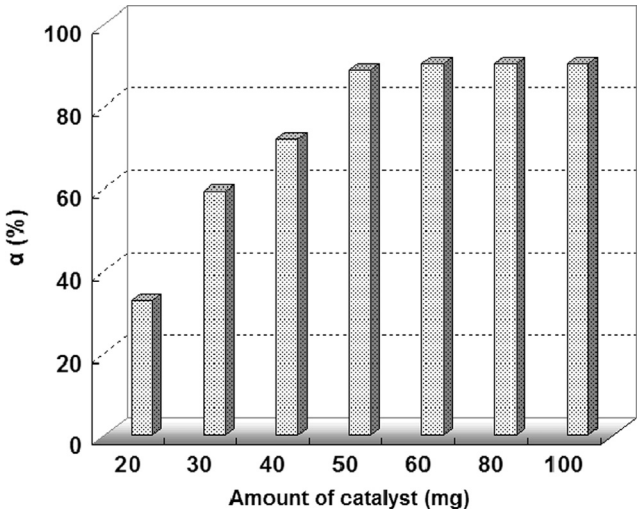

Fig. 7. Effect of NH-SRMS-S2-PPL amount on the lauric acid conversion rate.

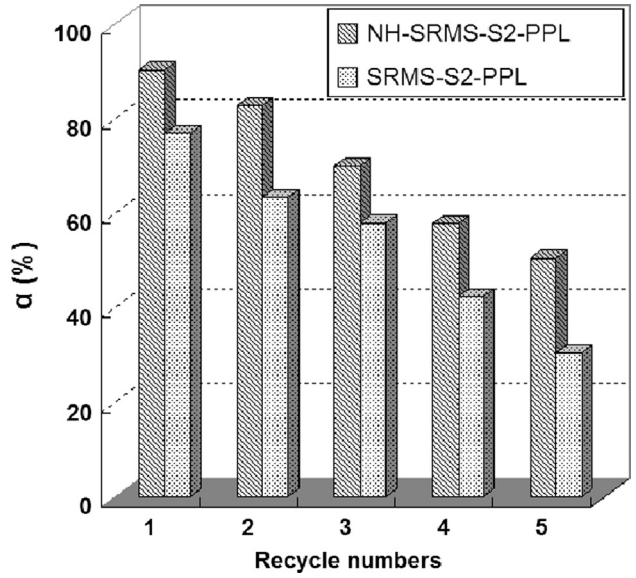

Fig. 8. Effect of recycle numbers on the lauric acid conversion rate.

was carried out using excess *n*-butanol. The esterification was investigated by varying different reaction parameters such as the amount of catalyst and reaction time to optimize the conditions for maximum yields. To study the effect of the amount of the catalyst, the reaction was carried out using different amounts of NH-SRMS-S2-PPL from 20 mg to 100 mg under otherwise similar conditions. The lauric acid conversion rate is reported in Fig. 7. The lauric acid conversion rate initially increased with increased amount of NH-SRMS-S2-PPL from 20 mg to 60 mg. The maximum conversion rate of 90.15% was obtained with further increased amount of NH-SRMS-S2-PPL; hence, 60 mg was deemed to be the optimum amount of catalyst. In the reaction involving SRMS-S2-PPL and NH-SRMS-S2-PPL, the maximum conversion rate of lauric acid was 76.85% and 90.15%. In addition, SRMS-S2-PPL or NH-SRMS-S2-PPL reusability studies were carried out to determine the stability of immobilized PPL during the reaction. The catalyst was separated from the reaction mixture by simple filtration, washed with a solvent, dried at room temperature, and reused as such. Fig. 8 shows that NH-SRMS-S2-PPL maintained 50% of its esterification conversion rate even after five cycles of use, whereas SRMS-S2-PPL maintained only 30%.

4. Conclusions

Mesoporous silica materials with a 2D mesostructure (*p6mm*) were successfully prepared with P123 and PVP as templates and used for the immobilization of PPL. Changes in PVP concentration and molecular weight caused mesoporous silica materials to vary between CRMS and SRMS with changes in length, width, and structure parameters. With increased PVP molecular weight, S_{BET} and V continuously decreased, and SRMS-S3 possessed larger D, d_{100}, and a_0, as well as better structural ordering compared with SRMS-S5 and CRMS-S6. Analysis of the effect of PVP concentration on the synthesis of mesoporous silica showed that SRMS-S2 was uniform without aggregation and had better structure ordering than CRMS-S1, SRMS-S3, and CRMS-S4. NH-SRMS-S2 also exhibited a higher loading amount than SRMS-S2. SRMS-S2-PPL and NH-SRMS-S2-PPL were able to promote the cycles of use and esterification of lauric acid with *n*-butanol, resulting in good conversion rates of 90.15% and 76.85%, respectively.

Acknowledgments

This work was supported by the National Natural Science Foundation of China (Grant No. 20976100, 51372124), the Natural Science Foundation of Shandong Province (Grant No. ZR2010BM013, ZR2011BQ009), and the Program for Scientific Research Innovation Team in Colleges and Universities of Shandong Province.

Appendix A. Supporting information

Additional SAXRD patterns, TEM Figures, N2 adsorption – desorption isotherms, corresponding BJH pore size distribution curves, and structure parameters on different samples and more detailed discussions of influence factors about immobilized PPL activities.

Supplementary data associated with this article can be found in the online version at http://dx.doi.org/10.1016/j.jssc.2014.03.004.

References

[1] K.R. Jegannathan, L. Jun-Yee, E.S. Chan, P. Ravindra, Fuel 89 (2010) 2272–2277.
[2] X. Li, X.Y. He, Z.L. Li, Y.D. Wang, C.Y. Wang, H. Shi, F. Wang, Fuel 92 (2012) 89–93.
[3] N. Pal, M. Paul, A. Bhaumik, J. Solid State Chem. 184 (2011) 1805–1812.
[4] Y.H. Wang, Y.T. Gan, R. Whiting, G.Z. Lu, J. Solid State Chem. 182 (2009) 2530–2534.
[5] A.A. Kiss, C.S. Bildea, J. Chem. Technol. Biotechnol. 87 (2012) 861–879.
[6] Y.C. Ardila, G.M.F. Pinto, A.B. Machado, M.R.W. Maciel, J. Chem. Eng. Data 55 (2010) 4592–4596.
[7] D.L. Wang, A. Nag, G.C. Lee, J.F. Shaw, J. Agric. Food Chem. 50 (2002) 262–265.
[8] C.F. Wang, G.W. Zhou, Y.Q. Xu, J. Chen, J. Phys. Chem. C 115 (2011) 22191–22199.
[9] G.W. Zhou, Y.J. Chen, S.H. Yang, Microporous Mesoporous Mater. 119 (2009) 223–229.
[10] I. Jang, K. Song, J.H. Park, M. Kim, D.W. Kim, S.G. Oh, Mater. Lett. 96 (2013) 214–217.
[11] J.M. Lee, Y.D. Jun, D.W. Kim, Y.H. Lee, S.G. Oh, Mater. Chem. Phys. 114 (2009) 549–555.
[12] C.L. Lee, R.B. Wu, C.M. Syu, Electrochem. Commun. 11 (2009) 270–273.
[13] H. Lin, X.H. Yan, X.F. Wang, J. Solid State Chem. 204 (2013) 266–271.
[14] Y.W. Tan, S. Srinivasan, K.S. Choi, J. Am. Chem. Soc. 127 (2005) 3596–3604.
[15] X.J. Shi, X. Chen, X.L. Chen, S.M. Zhou, S.Y. Lou, Y.Q. Wang, L. Yuan, Chem. Eng. J. 222 (2013) 120–127.
[16] S. Simone, A. Figoli, A. Criscuoli, M.C. Carnevale, A. Rosselli, E. Drioli, J. Membr. Sci. 364 (2010) 219–232.
[17] T.A. Nguyen, T.S. Jun, M. Rashid, Y.S. Kim, Mater. Lett. 65 (2011) 2823–2825.
[18] J. Kaewsaenee, P. Visal-athaphand, P. Supaphol, V. Pavarajarn, Ind. Eng. Chem. Res. 50 (2011) 8042–8049.
[19] Y.Y. Zhao, H.Y. Wang, X.F. Lu, X. Li, Y. Yang, C. Wang, Mater. Lett. 62 (2008) 143–146.
[20] H.Y. Wang, D.Y. Wu, D.Z. Li, Z.W. Niu, Y.Z. Chen, D.H. Tang, M. Wu, J.H. Cao, Y. Huang, Nanoscale 3 (2011) 3601–3604.
[21] D. Vu, Z.Y. Li, H.N. Zhang, W. Wang, Z.J. Wang, X.R. Xu, B. Dong, C. Wang, J. Colloid Interface Sci. 367 (2012) 429–435.
[22] B. Liu, K. Nakata, M. Sakai, H. Saito, T. Ochiai, T. Murakami, K. Takagi, A. Fujishima, Langmuir 27 (2011) 8500–8508.
[23] C.C. Huang, W. Huang, C.S. Yeh, Biomaterials 32 (2011) 556–564.
[24] Y.F. Zhu, J.L. Shi, H.R. Chen, W.H. Shen, X.P. Dong, Microporous Mesoporous Mater. 84 (2005) 218–222.
[25] N. Venkatathri, Solid State Commun. 143 (2007) 493–497.
[26] T. Yu, A. Malugin, H. Ghandehari, ACS Nano 5 (2011) 5717–5728.
[27] C.P. Tsai, Y. Hung, Y.H. Chou, D.M. Huang, J.K. Hsiao, C. Chang, Y.C. Chen, C.Y. Mou, Small 4 (2008) 186–191.
[28] X.L. Huang, L.L. Li, T.L. Liu, N.J. Hao, H.Y. Liu, D. Chen, F.Q. Tang, ACS Nano 5 (2011) 5390–5399.
[29] V. Brahmkhatri, A. Patel, Fuel 102 (2012) 72–77.
[30] S.D.T. Barros, A.V. Coelho, E.R. Lachter, R.A.S.S. Gil, K. Dahmouche, M.I.P.D. Silva, A.L.F. Souza, Renewable Energy 50 (2013) 585–589.
[31] A. Salis, M.S. Bhattacharyya, M. Monduzzi, J. Phys. Chem. B 114 (2010) 7996–8001.
[32] A.Z. Abdullah, N.S. Sulaiman, A.H. Kamaruddin, Biochem. Eng. J. 44 (2009) 263–270.
[33] F. Sevimli, A. Yılmaz, Microporous Mesoporous Mater. 158 (2012) 281–291.
[34] G.W. Zhou, G.Z. Li, J. Xu, Q. Sheng, Colloids Surf., A 194 (2001) 41–47.
[35] X.Y. Liu, L. Zhu, T. Zhao, J.F. Lan, W.F. Yan, H.X. Zhang, Microporous Mesoporous Mater. 142 (2011) 614–620.
[36] S. Kubo, K. Kosuge, Langmuir 23 (2007) 11761–11768.
[37] C. Bernal, M. Mesa, L. Sierra, Mater. Sci. Eng., C 32 (2012) 1380–1385.
[38] Z.W. Jin, X.D. Wang, X.G. Cui, Colloids Surf., A 316 (2008) 27–36.
[39] Y. Xu, D. Wu, Y.H. Sun, W.X. Chen, H.Z. Yuan, F. Deng, Z.H. Wu, Colloids Surf., A 305 (2007) 97–104.
[40] N.M.P.S. Ricardo, N.M.P.S. Ricardo, F.M.L.L. Costa, C. Chaibundit, G. Portale, D. Hermida-Merino, S. Burattini, I.W. Hamley, C.A. Muryn, S.K. Nixon, S.G. Yeates, J. Colloid Interface Sci. 353 (2011) 482–489.
[41] X.J. Shi, X. Chen, X.L. Chen, S.M. Zhou, S.Y. Lou, Y.Q. Wang, L. Yuan, Chem. Eng. J. 222 (2013) 120–127.
[42] C.I. Covaliu, I. Jitaru, G. Paraschiv, E. Vasile, S.Ş. Biriş, L. Diamandescu, V. Ionita, H. Iovu, Powder Technol. 237 (2013) 415–426.
[43] H. Aghayan, A.R. Mahjoub, A.R. Khanchi, Appl. Surf. Sci. 261 (2012) 14–20.
[44] W.H. Zhang, L. Zhang, J.H. Xiu, Z.Q. Shen, Y. Li, P.L. Ying, C. Li, Microporous Mesoporous Mater. 89 (2006) 179–185.
[45] S.F. Wei, J.S. Lian, Q. Jiang, Appl. Surf. Sci. 255 (2009) 6978–6984.
[46] Y.N. Xue, X.L. Ren, X.F. Zhai, M. Yu, Mater. Res. Bull. 47 (2012) 393–399.
[47] Z.D. Chen, X. Li, H.Y. He, Z.H. Ren, Y. Liu, J. Wang, Z. Li, G. Shen, G.R. Han, Colloids Surf., B 95 (2012) 274–278.
[48] C.J. Xu, D. Nie, H.Y. Chen, G.Z. Zhao, Y.Q. Liu, Mater. Lett. 110 (2013) 87–90.